Neuron, Volume *85*

Supplemental Information

Simultaneous Encoding of Odors by Channels with Diverse Sensitivity to Inhibition

Elizabeth J. Hong and Rachel I. Wilson

Inventory of Supplemental Information

Supplemental Item	Related Material	Explanation
Figure S1	Figure 1	shows that the spatial pattern of odor-evoked fluorescence changes in LNs are similar in different brains, whether GCaMP3 expression is driven by *GH298-Gal4* or *NP3056-Gal4*
Figure S2	Figure 2	a comparison of principal component analysis results for ORNs versus LNs, NP3056-LNs versus GH298-LNs, odor set 1 versus odor set 2, and experiments with four odors versus experiments with a single odor
Figure S3	Figure 4	demonstrates that increasing light intensities evoke increasing spike rates in ChR-positive LNs, but no response in ChR-negative LNs
Figure S4	Figure 6	repeats the same experiment and analysis as in Figure 6, but using two alternative fluorescent markers of LN morphology
Figure S5	Experimental Procedures	shows that a Gal4 line used in previous study labels antennal lobe PNs as well as LNs
Figure S6	Supplemental Experimental Procedures	shows that the kinetics of $\Delta F/F$ signals are similar across odors and glomeruli when GCaMP is expressed in LNs
Supplemental Table 1		data for all glomerulus-by-glomerulus measurements
Supplemental Experimental Procedures		provides additional detail regarding methods.

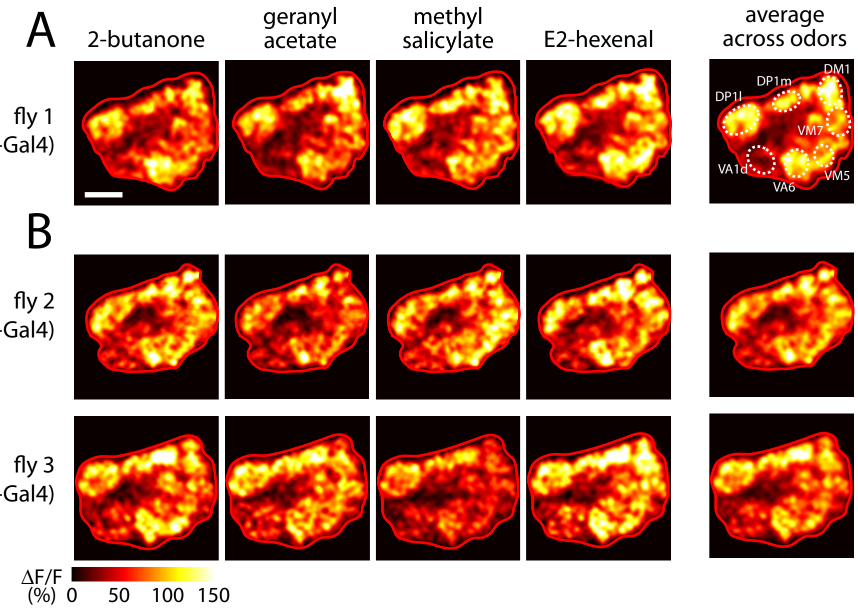

Figure S1. Spatial patterns of odor-evoked LN activity are similar across flies and Gal4 drivers.
(A) LN activity in a fly where GCaMP3 is expressed under the control of NP3056-Gal4 (imaged at the plane 24μm below the dorsal surface of the antennal lobe). Scale bar, 20μm. The response to each individual odor resembles the average across all four odors. In the average image, dotted lines mark the borders of seven glomeruli whose locations can be identified with high confidence. This data is reproduced from Figure 1C (bottom).
(B) Same as A, but for two flies where GCaMP3 is expressed under the control of GH298-Gal4.

Note the similarity between individual flies, and between different LN Gal4 lines. Subtle differences between responses to individual odors are due in part to the difference in the overall magnitude of the four odor responses at the given odor concentration used (Figure 3). Additional subtle differences are due to measurement noise, as evidenced by the fact that repeated trials with the same stimulus do not evoke identical responses (Figure S2H).

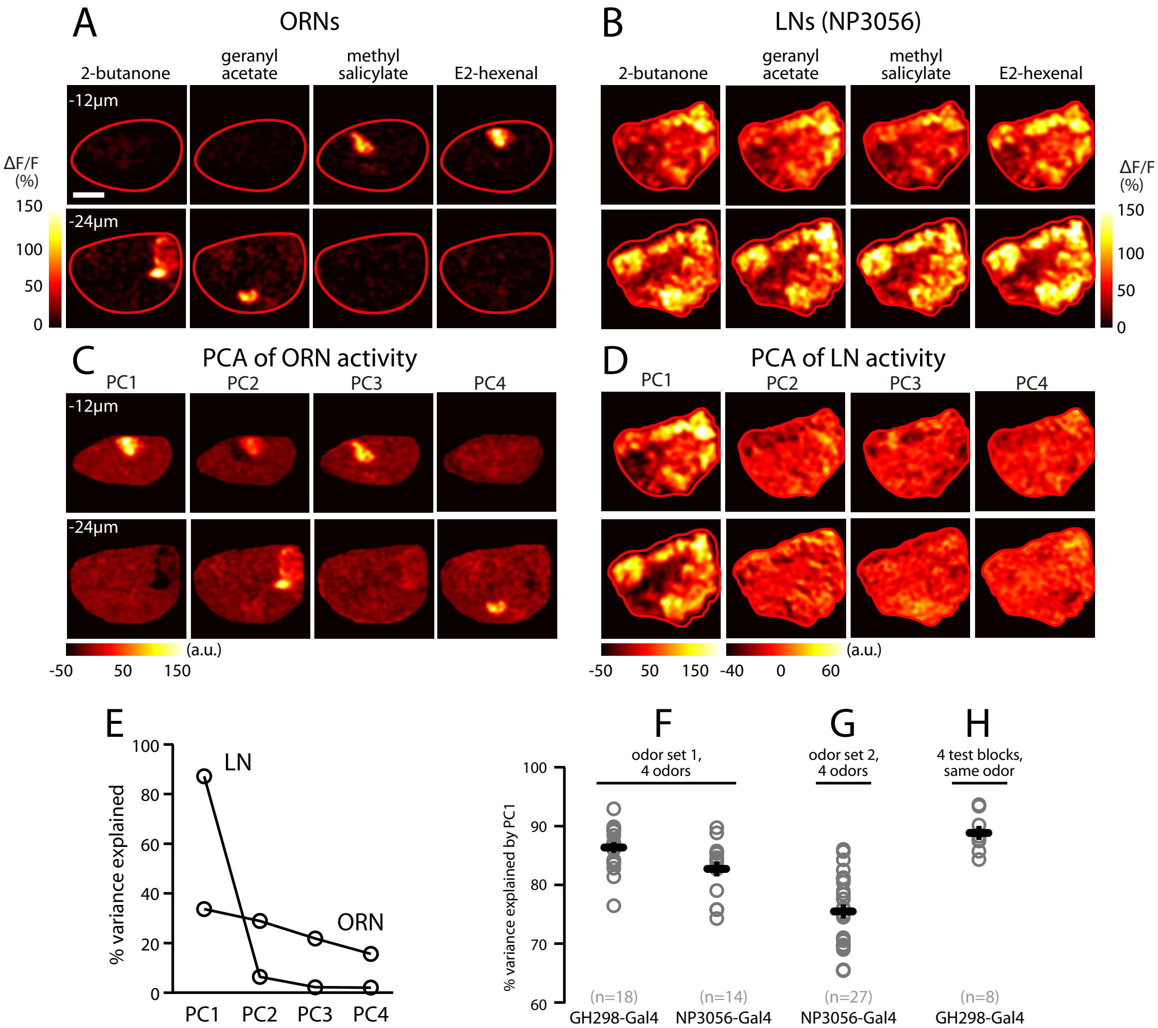

Figure S2. Principal component analysis (PCA) of ORN and LN activity.

(A) Odor-evoked activity in ORN axon terminals (reproduced from Figure 1A). Scale bar, 20 µm.

(B) Odor-evoked activity in LNs (reproduced from Figure 1C), at the same two imaging planes as (A).

(C) Principal components of the ORN activity patterns from the experiment in (A). Note that all four PCs contain structures corresponding to activated glomeruli. This occurs because the four odors activate independent activity patterns. (For panels (C) and (D), the input to the PCA was a set of four odor-evoked images, one per odor, with the two imaging planes concatenated to create a single image. Panels (C)-(E) are the only places in this study where imaging planes were concatenated for PCA; this was done to allow a direct comparison between ORN and LN PCA, since two planes are needed to fully describe the ORN responses to the four odors.)

(D) Same as (C) for the LN experiment in (B). Note that each odor response resembles a scaled version of PC1. PC2-PC4 contain mainly noise (as evidenced by the fact that they have little structure on the spatial scale of a glomerulus).

(E) Percent variance explained by each PC for these two experiments. For LNs, almost all the variance across odors is explained by a single PC, indicating that each odor response represents a scaled version of the average across odors. By contrast, for ORNs, each of the four PCs captures a substantial portion of the variance across odor-evoked activity patterns.

(F) Percent variance explained by PC1 for LN experiments with odor set 1. Circles are individual experiments; black bar is the mean. PC1 accounts for much of the variance across odors (~85%). Similar results were obtained with the two LN Gal4 lines.

(G) Percent variance explained by PC1 for LN experiments with odor set 2. In this case, PC1 accounts for a smaller percentage of the variance across odors, (as compared to experiments with odor set 1, $p<0.05$, Tukey-Kramer HSD) consistent with our finding that three of the four stimuli in odor set 2 elicit extra LN activity in their cognate glomeruli (Figure 2B-C). This result demonstrates that PCA is a sensitive method for detecting a case where LN activity is independently modulated in different glomeruli.

(H) To understand the origin of the variance not explained by PC1 in the experiments using odor set 1, we performed additional experiments where we presented the same stimulus repeatedly for the entire experiment. Whereas in all other experiments we presented 4 stimuli for 4 trials each, we here presented the same stimulus for 16 consecutive trials, and then divided this into four arbitrary blocks of 4 trials each. In this analysis, the amount of variance captured by PC1 was typically 85-90%. The unexplained variance (the remaining 10 -15%) must be due to trial-to-trial fluctuations in measured LN odor responses, because it cannot be due to differences between stimuli. This control shows that PC1 explains almost all the explainable variance in the LN experiments -- i.e., all the variance which is due to the stimulus rather than the noise.

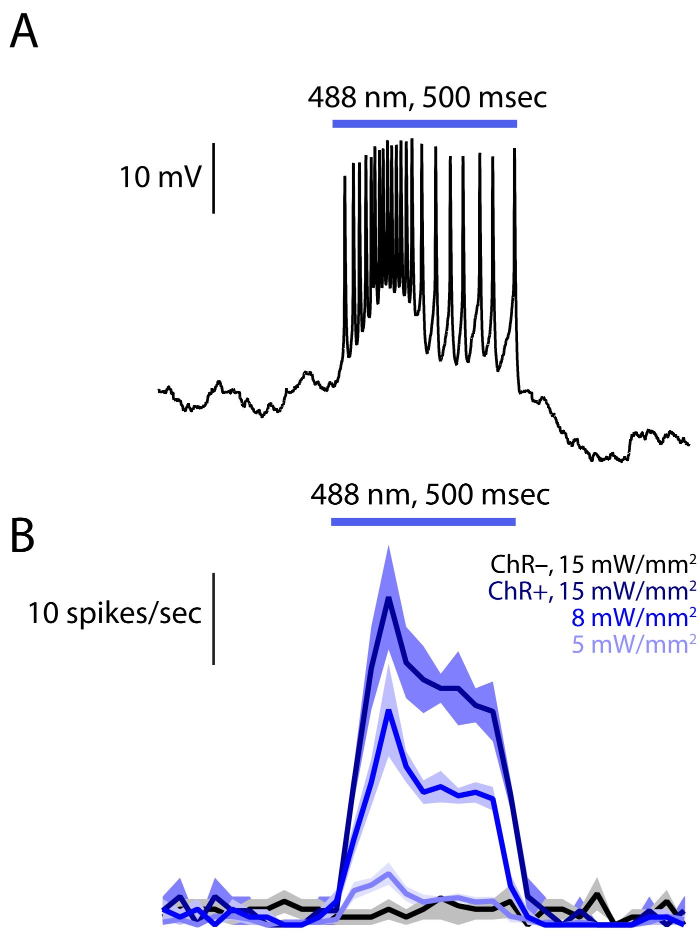

Figure S3. Optogenetic activation of LN firing.
(A) Current clamp recording of light-evoked action potentials in an individual ChR+ LN (15 mW/mm^2).
(B) Increasing light intensity elicits increasing spike rates in ChR+ LNs, but no response in ChR- LNs. Peri-stimulus time histograms show mean spike rate recorded in current-clamp mode (in 50 msec bins), ± SEM across experiments (n=5).

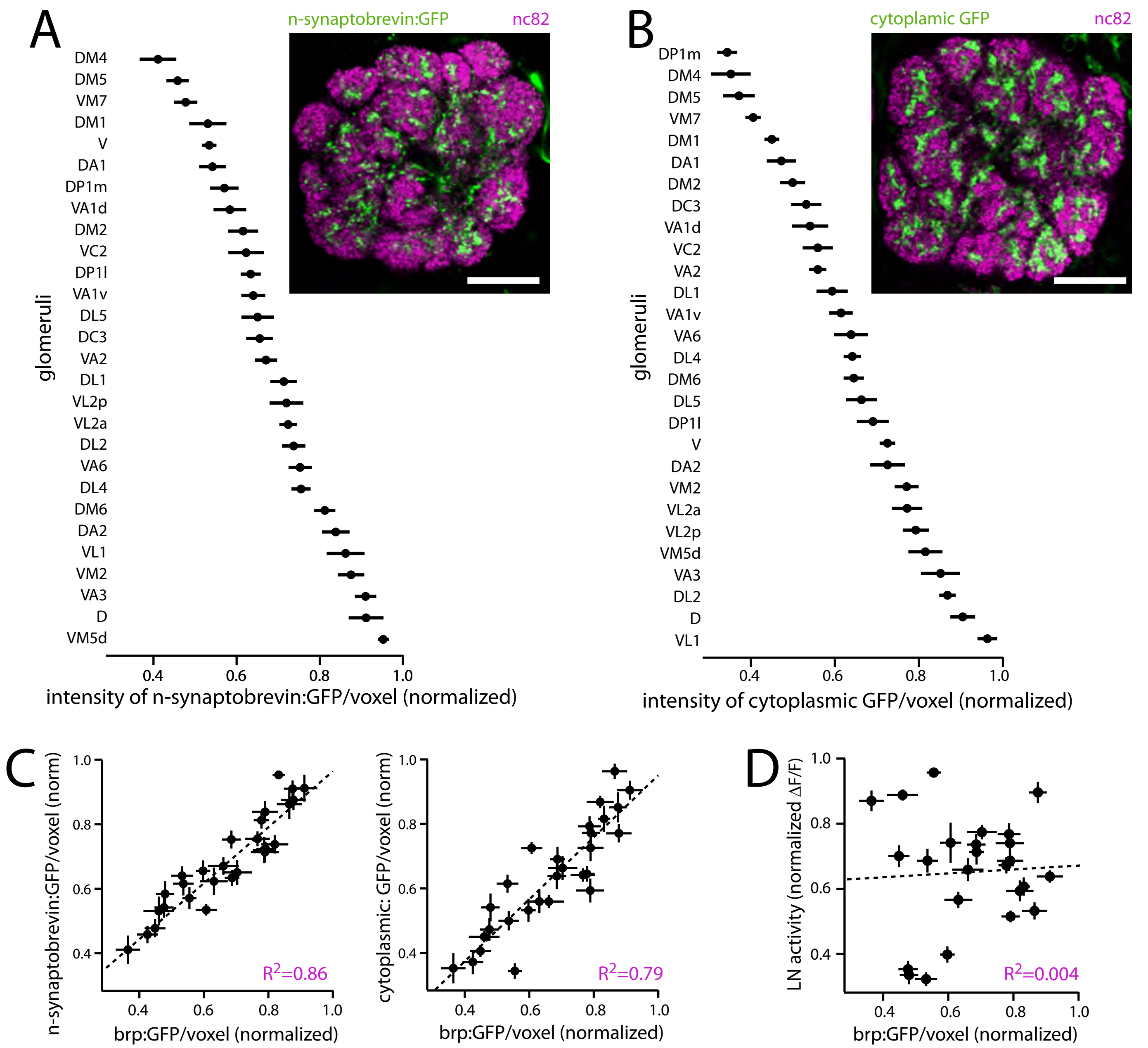

Figure S4: Variations across glomeruli in the density of different LN anatomical markers are strongly correlated, but there is no correlation between LN release sites and LN calcium signals.

(A) Measurements of n-synaptobrevin:GFP signal per unit glomerular volume. Like brp:GFP, n-synaptobrevin:GFP is a marker of presynaptic release sites. Data are the mean of 8 measurements, ± SEM. Inset shows a confocal section through the antennal lobe (genotype: *UAS-nsyb:GFP/SM6; NP3056-Gal4/+*). The antennal lobe is imaged at an equivalent frontal plane as in Figure 6A. The brain is co-stained with the nc82 antibody to visualize neuropil boundaries. Scale bar, 20 µm.

(B) Same as (A) but for a marker of total LN neurite volume (cytoplasmic GFP) (genotype: *UAS-2X-eGFP/NP3056-Gal4*).

(C) Variations across glomeruli in the density of brp:GFP are highly correlated with variations in the density of n-synaptobrevin:GFP and cytoplasmic GFP. (Each datapoint represents a different glomerulus, mean ± SEM.) This finding implies that, on average, neurotransmitter release sites are arranged with a roughly equal density per unit cytoplasm, although there may be variations in the density of release sites within individual LNs (Chou et al., 2010).

(D) Average LN activity (%ΔF/F), as quantified in Figure 1E, is not significantly correlated with the density of LN release sites ($p = 0.77$). Note that ΔF/F measurements are already normalized for resting fluorescence (F), which should correct for variations across glomeruli in the density of LN innervation; thus, there is no necessary relationship between ΔF/F and innervation density. Each point is a different glomerulus, mean ± SEM.

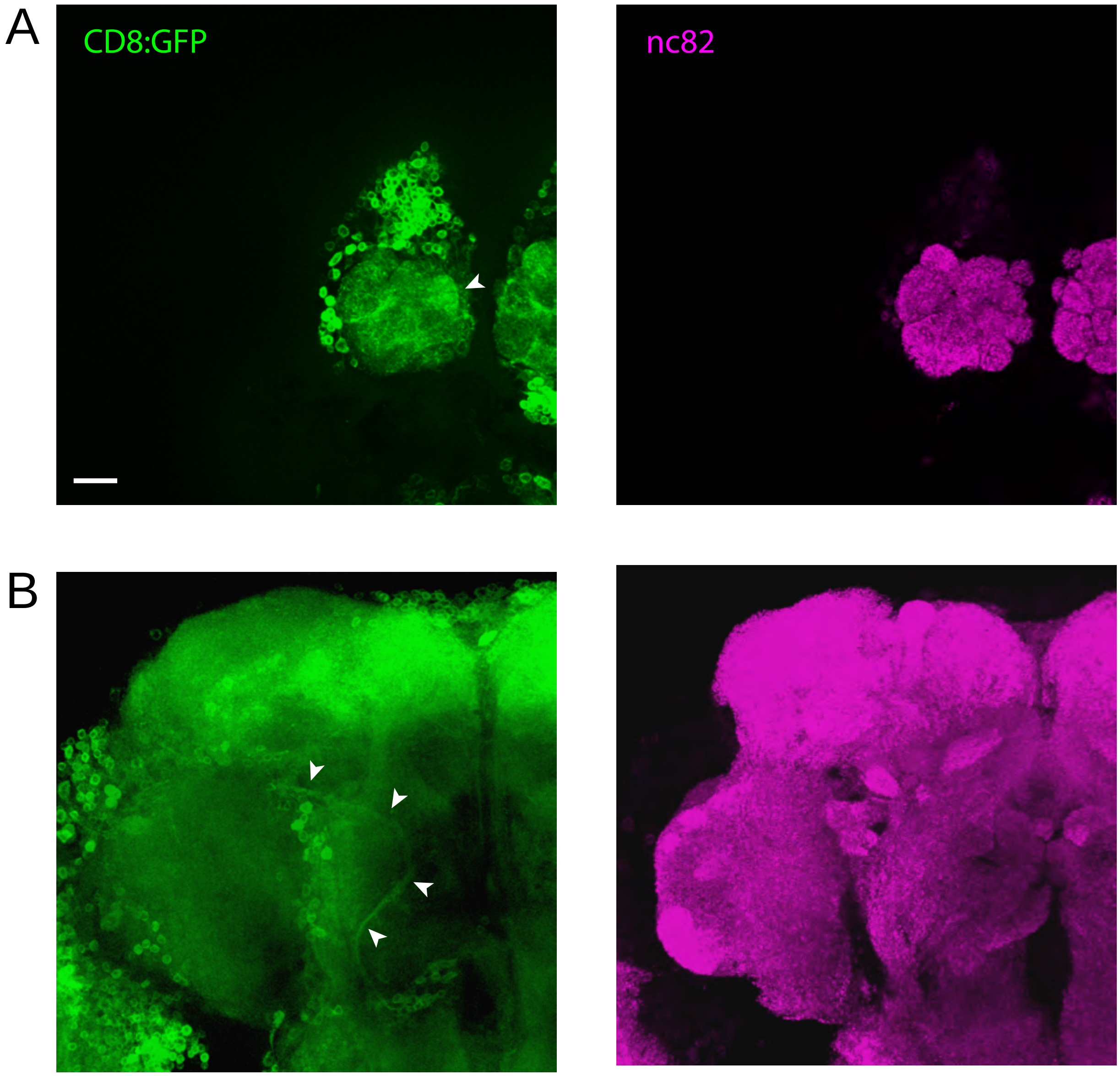

Figure S5. *Gad1-Gal4* labels ventral PNs (vPNs) in the antennal lobe.
(A) Maximum intensity projection of 10 confocal planes spanning the anterior region of the antennal lobe in an animal expressing CD8:GFP under the control of Gad1-Gal4 (genotype: *Gad1-Gal4/[CyO]; UAS-CD8:GFP/+*). Brains were co-stained with anti-CD8 (green) and nc82 (magenta) antibodies. Scale bar, 20 µm. Note the dense CD8 labeling of some glomeruli, which resembles the dendritic tufts of some vPNs (Jefferis et al., 2007; Lai et al., 2008). (B) Same as (A), but for 16 confocal planes spanning the region immediately posterior to the antennal lobe. The arrowheads mark the axon bundle that leaves the antennal lobe and projects via the medial antennocerebral tract to the lateral horn. This is the tract that carries the axons of vPNs (Jefferis et al., 2001, 2007; Lai et al., 2008). Because vPNs are GABAergic (Wilson and Laurent, 2005; Jefferis et al., 2007), it is expected that these PNs express Gal4 in the Gad1-Gal4 line.

Jefferis, G.S., Marin, E.C., Stocker, R.F., and Luo, L. (2001). Target neuron prespecification in the olfactory map of Drosophila. Nature 414, 204-208.

Jefferis, G.S., Potter, C.J., Chan, A.M., Marin, E.C., Rohlfing, T., Maurer, C.R., Jr., and Luo, L. (2007). Comprehensive maps of Drosophila higher olfactory centers: spatially segregated fruit and pheromone representation. Cell 128, 1187-1203.

Lai, S.L., Awasaki, T., Ito, K., and Lee, T. (2008). Clonal analysis of Drosophila antennal lobe neurons: diverse neuronal architectures in the lateral neuroblast lineage. Development 135, 2883-2893.

Wilson, R.I., and Laurent, G. (2005). Role of GABAergic inhibition in shaping odor-evoked spatiotemporal patterns in the Drosophila antennal lobe. J Neurosci 25, 9069-9079.

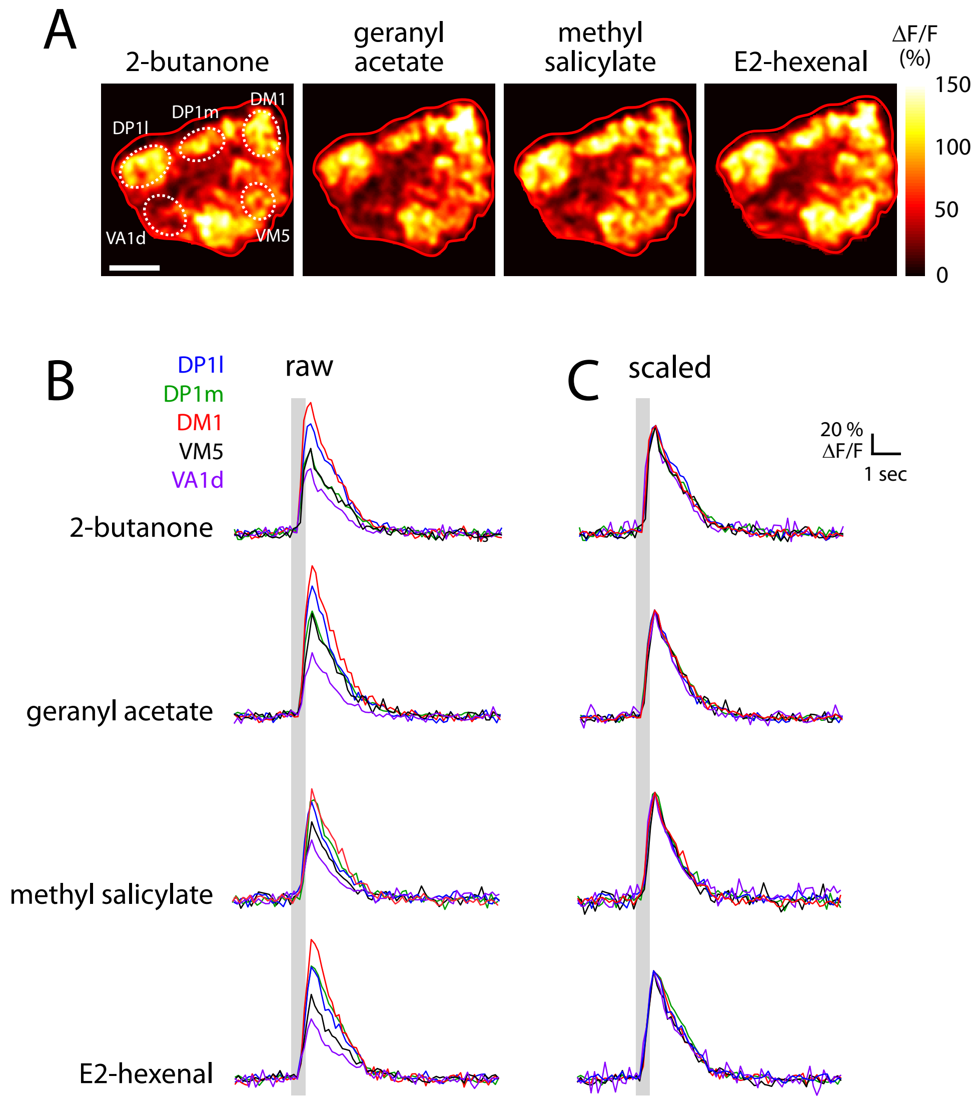

Figure S6. The kinetics of odor responses are similar across glomeruli.
(A) Odor-evoked spatial patterns of LN activity, imaged at the plane 24µm below the dorsal surface of the antennal lobe (reproduced from Figure S1A). Odor stimuli are as described in Figure 1. Scale bar, 20 µm.
(B) Time course of odor-evoked calcium transients in the five indicated glomeruli, averaged across four presentations of each odor stimulus. Glomerular ROIs were determined as described in Experimental Procedures.
(C) Same as (B), but with each calcium response normalized to its peak value. Note that the kinetics of odor-evoked calcium signals are very similar across different glomeruli and across different odors.

SUPPLEMENTAL EXPERIMENTAL PROCEDURES

Flies

Gal4 drivers. The Gal4 drivers used in this study have been previously characterized as follows. *pebbled-Gal4* labels larval and adult ORNs (Sweeney et al., 2007). *Mz19-Gal4* labels DA1 and VA1d PNs (Berdnik et al., 2006). *NP3481-Gal4* labels VM7, VM2, DL5, and DM6 PNs (Olsen et al., 2007). *GMR46E07-Gal4*(attP2) (Pfeiffer et al., 2008) labels VA3 PNs, along with several other PN types (data not shown). *NP3056-Gal4* and *GH298-Gal4* label large subsets of GABAergic LNs (Chou et al., 2010). MARCM analysis of *GH298-Gal4* has shown that it also drives Gal4 expression in small numbers of ORNs and PNs (Chou et al. 2010), but we find that expression is much lower than that in LNs. We used confocal microscopy to examine the antennal lobes of flies expressing CD8:GFP under the control of *GH298-Gal4*, using immunofluorescence to amplify CD8 signal (Wilson and Laurent, 2005), and using gain settings where the signal in LNs is saturated. We found that CD8:GFP is undetectable in the antennal nerve and the midline commissure (where ORN axons run), and also undetectable in the antennocerebral tract (where PN axons run) (data not shown).

We also examined *Gad1-Gal4*, which was used to perform optical imaging of LNs in a previous study (Ng et al., 2002). That study reported that odor stimuli elicit sparse and odor-specific patterns of LN activity, which is inconsistent with our results. We found that *Gad1-Gal4* drives expression in some PNs as well as LNs (Figure S5), which may partly explain the findings of Ng et al. To avoid this confound, we selected one line (*NP3056-Gal4*) whose antennal lobe expression is cleanly restricted to LNs. We also used a second line (*GH298-Gal4*) which is less clean, but even here ORN and PN signals were not detectable under conditions where we could easily see PN expression in the *Gad1-Gal4* line.

UAS transgenes. The Gal4-responsive UAS transgenes used in this study have been previously described as follows: *UAS-GCaMP3.0* (attP40) (Tian et al., 2009, Bloomington Drosophila Stock Center (BDSC) 32116); *UAS-bruchpilot:GFP (II)* (Schmid et al., 2008, BDSC 36291); *UAS-nsyb:GFP* (*III*) (Estes et al., 2000); *UAS-2X-eGFP (II)* (Halfon et al., 2002, BDSC 6874); *UAS-ChR2:YFP-C (II)* and *UAS-ChR2:YFP-B (III)* (inserts "C" and "B" from Hwang et al., 2007); *UAS-CD8:GFP* (Lee and Luo, 1999). The *shakB*^{2} mutant and its effects on lateral excitation in the antennal lobe have been previously described in Baird et al. (1990) and Yaksi & Wilson (2010).

Odor delivery

All odor concentrations are reported as v/v dilutions in paraffin oil (J.T. Baker, VWR #JTS894) as the solvent, and each 20-ml odor vial (VWR, VW74511-20) contained a final volume of 5 ml of diluted odor in paraffin oil. Fresh odor dilutions were made every four days. Odors were delivered essentially as previously described (Bhandawat et al., 2007) with the following modifications. A constant stream of charcoal-filtered air (2.2 ml/min) was directed at the fly, with a small portion of the stream (0.2 ml/min) passing through the headspace of a control vial filled with only solvent prior to joining the carrier stream (2.0 ml/min). When triggered by an external voltage command, a three-way solenoid valve redirected the small portion of the stream (0.2 ml/min) from the solvent-only vial through the headspace of the odor vial for 500 msec, thus further diluting the odor by 10-fold prior to final delivery to the animal. The solvent-only vial and the odor vial entered the carrier stream at the same point, 12 cm from the end of the tube. The tube opening measured 4 mm in diameter and was positioned one cm away from the fly.

For experiments in Figures 1 and 2, the order of odor presentation was randomized for each imaging plane, and the entire odor set was presented before moving to another imaging depth. This configuration was chosen to minimize any differences in imaging position across odor stimuli for each imaging plane sampled. For experiments in Figure 3, the stimuli within each odor concentration series were presented in order from least to most concentrated, and the order in which the odor series were presented was randomized at each imaging plane. Each odor stimulus was presented in a block of four trials (for imaging LN activity) or three trials (for imaging ORN activity), with an inter-trial interval of 90 s. The odor delivery tube was flushed with clean air for 2 minutes when changing between odors.

For LFP (local field potential) recordings from the antenna or palp, each odor stimulus was presented in a block of 4-6 trials, with an inter-trial interval of 45 s. The stimuli within each odor concentration series were presented in order from least to most concentrated, and the order in which the odor series were presented was randomized at each recording site. The odor delivery tube was flushed with clean air for 2 minutes when changing between odor series.

Calcium imaging of odor-evoked activity

All calcium imaging experiments were performed on female flies aged 4-5 weeks post-eclosion. Aging the flies increased levels of GCaMP3 expression and improved signal strength. Flies were reared at 25°C, collected as virgins at eclosion, and maintained in small cohorts in vials at room temperature (20-22°C) under laboratory lighting conditions.

The experimental preparation for imaging was essentially as described for electrophysiological recordings (Wilson et al., 2004) with slight modifications. In brief, the animal was head-fixed into a small custom-cut window in a thin sheet of foil, and the dorsal cuticle of the head capsule was removed to expose the antennal lobes. The head was tilted as far back toward the body as was possible while still preventing saline from leaking onto the antennae, which were tucked beneath the plane of the foil and kept dry. This position allowed us to acquire horizontal imaging planes through the dorsal-ventral extent of the antennal lobes. Care was taken to remove all fat, air sacs, and trachea both above and below the antennal lobe(s) of interest to reduce light scattering.

Imaging experiments were performed at room temperature, and the brain was constantly perfused with saline containing (in mM): 103 NaCl, 3 KCl, 5 N-Tris(hydroxymethyl)methyl-2-aminoethane-sulfonic acid, 8 trehalose, 10 glucose, 26 $NaHCO_3$, 1 NaH_2PO_4, 1.5 $CaCl_2$, and 4 $MgCl_2$ (pH 7.3, osmolarity adjusted to 270–275 mOsm). The saline was bubbled with 95% O_2/5% CO_2 and circulated in the bath at ~2-3 ml/min. Two-photon fluorescence of GCaMP3 was excited with 925-nm light and collected with a custom-built 2-photon laser scanning microscope. The microscope and data acquisition was controlled by ScanImage r3.0 (Pologruto et al., 2003; Janelia Research Campus, Ashburn, VA).

Antennal lobes were imaged from the dorsal side. A single imaging trial consisted of 120 single-pass frames acquired at a resolution of 128×128 pixels and a nominal frame rate of 7.8 Hz. Odor was delivered for 500 msec at frame 40. At the beginning of an experiment and subsequently at the end of every stimulus block (about every 6 minutes), flies were challenged with a strong test odor (2-heptanone, 10^{-3} dilution) as a positive control for robust olfactory function, and we subsequently performed data analysis only on those experiments where: 1) the average response was >60% $\Delta F/F$, and 2) the response did not change >15% from baseline over the course of the experiment.

By imaging odor-evoked calcium signals in the axons of ORNs terminating in the antennal lobe, we determined that four imaging planes which sample the dorsal-ventral axis of the antennal lobe at 12-μm intervals (-12 μm, -24 μm, -36 μm, -48 μm relative to the dorsal surface of the antennal lobe neuropil) cover the glomeruli activated by all of the odors in our two “private” odor sets. Furthermore, no significant odor-evoked ORN signals were observed in between these imaging planes for any of the stimuli in either odor set, so we focused our experiments on these four imaging planes. The stimuli in odor set 1 (2-butanone, 5×10^{-6} [glomerulus VM7]; geranyl acetate, 10^{-5} [VA6]; methyl salicylate, 5×10^{-5} [DL1]; E2-hexenal, 10^{-6} [DL5]) activated glomeruli all contained in either the -12 μm or -24 μm imaging planes. In pilot experiments, we also imaged throughout the antennal lobe at ~6 μm intervals at planes dorsal, ventral, and intermediate to these two planes, and we observed qualitatively similar results. Therefore, we focused the experiments with odor set 1 on the -12 μm and -24 μm imaging planes, although in some experiments, we collected LN data at -12 μm and -36 μm, or -24 μm and -36 μm. Qualitatively similar results were observed regardless of the imaging planes we selected. The stimuli in odor set 2 (geosmin, 1% [DA2]; phenylacetaldehyde, 10^{-5} [VL2a]; CO_2, 5% [V]; methyl acetate, 10^{-5} [DM4]) evoke ORN calcium signals in all four imaging planes, each corresponding to one of the glomeruli innervated by an active ORN type. Therefore, we collected both ORN and LN data for odor set 2 at all four imaging planes. Typically, due to constraints on the amount of time a preparation remained healthy (~45-60 min), two imaging planes were evaluated in an individual experiment.

Calcium imaging of optogenetically-evoked activity

Optogenetically-evoked activity was imaged in the -12 μm, -24 μm, and -36 μm imaging planes essentially as described above. A 1-sec pulse of blue light was delivered from the tip of a fiber optic cannula (105-μm core, 0.22 NA, Thorlabs, Newton, NJ) butt-coupled to a 5W, 470-nm, high current LED (SF30, Smart Vision Lights, Muskegon, MI) via a fiber optic patch cable (200-μm core, Thorlabs). The fiber optic cannula was mounted with its long axis at approximately 45° from the horizontal. The tip of the fiber optic cannula was then lowered into the saline using a motorized actuator and positioned ~250 μm from the surface antennal lobe, with the long axis of the cannula directed toward the center of the antennal lobe. The collection photomultiplier tubes on the two-photon microscope were mechanically shuttered for the duration of the LED pulse to protect them from intense light. Light intensity was controlled by delivering varying levels of voltage to the LED. Odor stimuli were delivered to the antennae in the same manner as in all other experiments with odors, allowing for the comparison of light- and odor-evoked responses in the same brain.

Local field potential recordings

LFP measurements were performed as previously described (Olsen et al., 2010). Antennal LFPs were averaged from two recordings, one at a proximal and one at a distal site in the third antennal segment, as described previously. Palp LFPs were measured at a single recording site in the middle of the palp. Figure 3B shows responses from the antenna only. Total ORN input was calculated as a weighted combination of antennal and palp LFPs according to the approximate proportion of ORNs each structure houses (ORN input = $0.9 \times LFP_{antennal} + 0.1 \times LFP_{palp}$). The standard errors in the $LFP_{antennal}$ and LFP_{palp} measurements were propagated using standard methods:

$$\partial \mathrm{ORNinput} = \sqrt{(0.9\partial \mathrm{LFP}_{antennal})^2 + (0.1\partial \mathrm{LFP}_{palp})^2}$$

Immunohistochemistry

Biocytin fills were processed as previously described (Wilson et al., 2004). In brief, brains were fixed for 14 min at room temperature in 4% paraformaldehyde, incubated overnight in mouse nc82 (1:40, Developmental Studies Hybridoma Bank), and subsequently incubated overnight in Alexa Fluor 568 streptavidin conjugate (1:1000, Molecular Probes) and Alexa Fluor 633 goat anti-mouse (1:500, Molecular Probes). Brains were mounted and imaged in Vectashield mounting medium (Vector Labs).

For quantification of LN innervation and presynaptic release sites, brains were lightly fixed for 8 min in 3% paraformaldehyde, incubated in mouse nc82 (1:25) for 4-5 hours, and then incubated in Alexa Fluor 633 goat anti-mouse (1:250) for two hours. All steps were performed at room temperature, and brains were immediately imaged after the final wash step. Fluorescence arising from LNs (bruchpilot:GFP, n-synaptobrevin:GFP, or cytoplasmic GFP) originates from direct fluorescence of the protein without amplification from immunostaining. In pilot experiments, we amplified GFP signal using a chicken anti-GFP antibody (A10262, Invitrogen) and observed brighter, but qualitatively similar results. Confocal z-stacks spanning the entire volume of the antennal lobe were collected on a Zeiss Meta-510 microscope at 1μm z-intervals using a 63× oil-immersion lens.

Electrophysiology

Whole-cell patch-clamp recordings were performed as previously described (Wilson et al., 2004). The external recording solution was the same saline used for the calcium imaging experiments (see above). The internal patch-pipette solution for voltage clamp recordings contained (in mM): 140 cesium aspartate, 10 HEPES, 4 MgATP, 0.5 Na_3GTP, 1 EGTA, 1 KCl, and 13 biocytin hydrazide (pH 7.3, osmolarity adjusted to ~265 mOsm). The saline was bubbled with 95% O_2/5% CO_2, equilibrated at a pH of 7.3, and was circulated at ~2-3 ml/min. For current-clamp recordings, cesium was replaced with an equimolar substitution of potassium. Cell soma were targeted for recording under a 40× water-immersion objective. In some cases, recordings were facilitated by expressing GFP in target cells and visualizing GFP-positive somata under conventional epifluorescence illumination. In voltage-clamp recordings, PNs were held at a command potential of -60 mV. In current-clamp recordings, LNs were held between -50 and -45 mV by injecting a small amount of hyperpolarizing current (Chou et al., 2010; Gouwens and Wilson, 2009). Input resistance, computed as the membrane potential change resulting from a negative current step injected into the soma divided by the current step, was monitored throughout the experiment. The experiment was rejected if the cell's input resistance changed by more than 15% over the course of the recording. Recordings were acquired with an Axopatch 200B amplifier, low-pass filtered at 2 kHz, and digitized at 10 kHz. Data were acquired in Igor Pro and analyzed with custom scripts. A maximum of one neuron was recorded on each side of the brain to allow unambiguous identification post hoc by biocytin-streptavidin labeling. For some neurons, identification of the PN was facilitated by a PN's characteristic response profile to a panel of odorants.

Optogenetics and light calibration

Flies used for optogenetic experiments were cultured on conventional cornmeal medium supplemented with potato flakes rehydrated 1:1 (v/v) in an aqueous solution of all-trans-retinal (140 μM). All-trans-retinal was prepared as a 35 mM stock in ethanol and stored at –20°C. 20 μl of 35 mM all-trans-retinal was diluted in 1 tsp (4.9 mL) of water, and used to rehydrate 1 tsp of potato flakes. The parental cross that generated experimental flies was carried out in the dark on all-trans-retinal-supplemented medium, and newly eclosed experimental flies were maintained in the dark for 2 days (for electrophysiology) or 24-30 days (for imaging), also on all-trans-retinal medium.

For the experiments described in Figure 4C-F and Figure 5, the blue light used to activate channelrhodopsin-2 was generated from a 100W Hg arc lamp, band-pass filtered at 460-500 nm, and delivered to the specimen focused through a 40× water-immersion objective. The power density was varied using a fine series of neutral density filters and was calibrated using an optical power meter (Newport 1916-C) with the photodetector (818P-015-19) positioned behind a pinhole aperture placed at the level of the specimen. Because the effective power density at the specimen drifted slightly over days to weeks, the calibration procedure was repeated daily to achieve the same light intensities each day. Light pulses were delivered with a mechanical shutter (Uniblitz) that was driven by an external TTL pulse. Each light intensity was presented for 5-6 trials at an interval of 90 sec between trials. We included in our analysis the data collected using light intensities ranging from 2-22 mW/mm^2. Data using higher light intensities were collected in pilot experiments to identify the limit at which light starts to produce artifactual responses in control flies – we found this to be around intensities >54 mW/mm^2.

GABA uncaging

For GABA uncaging experiments, the entire electrophysiology rig and the tubing containing the saline were shielded from room lights. Prior to washing in DPNI-caged GABA (Trigo et al., 2009), we always collected a baseline response in saline to a brief pulse of the highest intensity UV light to be used in the experiment, in order to verify that the light had no effect on sEPSCs. Subsequently, 2.5-mL of 100 μM DPNI-caged GABA in oxygenated saline was re-circulated through the bath using a peristaltic pump. Wash-in of DPNI-caged GABA did not change spontaneous synaptic activity (quantified by taking the standard deviation of the current trace, see Analysis below), as compared to the baseline period in saline, across all experiments (saline vs. DPNI-GABA: 4.27±0.13 pA vs. 4.29±0.15 pA, p=0.94, paired t-test). This observation indicates

DPNI-caged GABA at this concentration does not act on GABA receptors to change sEPSC activity prior to photolysis.

The UV light pulse used for GABA uncaging was generated by mechanically shuttering the output from a 100W Hg arc lamp, band-pass filtered at 330-385 nm. The light intensity was controlled and calibrated as described above (under "Optogenetics and light calibration**")**. Each light intensity was presented for 5-6 trials at an interval of 90 sec between trials. We included in our analysis the data collected using light intensities ranging from 1-11 mW/mm^2. Data using higher light intensities were collected in pilot experiments to identify the limit at which light starts to produce artifactual responses in control flies – we found this to be around intensities >28 mW/mm^2. For a subset of experiments, we washed in GABA receptor antagonists (5 μM picrotoxin, 50 μM CGP54626) at the end of the experiment to confirm that the effect of light on sEPSC activity depended on GABA receptor function.

We found no significant correlation between glomerular depth and sensitivity to GABA (R^2=0.05, p=0.33). The depth of each glomerulus was measured from confocal stacks of six antennal lobes, stained with the nc82 antibody (see Immunohistochemistry). Depth was measured from the dorsal surface of the antennal lobe (determined from the maximum intensity z-projection of the stack) to the center of each glomerulus. This result implies that both light and GABA have approximately uniform access to all glomeruli.

Analysis

Glomerulus VC3 was excluded from our analyses because the odor response profiles of VC3 PNs differed dramatically in recordings from different brains (in one case, even from two VC3 PNs recorded on the right and left sides of the same brain). Because our goal was to compare how variation in the mechanisms underlying inhibition compares to the functional properties of glomeruli, we can only make meaningful conclusions about glomeruli that have stereotyped functional properties (i.e. odor tuning).

However, including VC3 in our analyses did not qualitatively change any of our conclusions. With VC3 included, sensitivity to LN activation is still highly glomerulus-specific (Figure 5D, one-way ANOVA w/VC3 included: p=0.0003). Likewise, sensitivity to GABA is also glomerulus-specific with VC3 included (Figure 8C, one-way ANOVA w/VC3 included: p=$4x10^{-8}$). In addition, with VC3 data included, sensitivity to LN activation is still highly correlated with sensitivity to GABA (Figure 8D, R^2=0.65, p=0.001 w/VC3 included, permutation test). Data from VC3 PNs are presented in a separate worksheet in Supplemental Table 1.

Calcium imaging and principal component analysis (PCA)

Within the time resolution of our sampling, the kinetics of the odor-evoked calcium signal were similar across glomeruli, both within a single trial and between different odors (Figure S6). Thus, we focused our analysis on the spatial pattern of the peak calcium signal in each trial.

Each trial comprised 120 frames acquired at 7.8 Hz, with the stimulus being delivered at frame 40. Calcium transients ($\Delta F/F$) were measured as changes in fluorescence (ΔF) normalized to the fluorescence during the baseline period (F, averaged over frames 5 to 35). Normalizing in this manner corrects for trivial effects of small drifts in imaging plane depth, variations in GCaMP concentration, and variations in LN innervation density; there is thus no necessary relationship between $\Delta F/F$ and LN innervation density. A Gaussian low-pass filter of size 5×5 pixels was applied to raw $\Delta F/F$ signals prior to any analysis. The frame containing the peak response was identified by plotting the average %$\Delta F/F$ in an ROI drawn around the antennal lobe, as a function of frame number. The peak calcium signal for each trial was computed as the average of three consecutive frames centered on the frame of peak response. For each odor stimulus, data was pooled by averaging the peak odor-evoked calcium signal (%$\Delta F/F$) across three (ORN imaging) or four (LN imaging) odor presentation trials.

Each imaging plane in each brain was analyzed by a separate PCA. PCA was computed using the "princomp" function in Matlab (R2013b). The four inputs to each PCA were the %$\Delta F/F$ values of pixels circumscribed by the antennal lobe region of interest (ROI) from the four trial-averaged images corresponding to the four odor stimuli used in that experiment. The same ROI was applied to each of the four images collected at the same plane in the same experiment. Inputs were centered by mean-subtraction, but not standardized, since they were all collected in the same units. For display purposes, output PCs were reshaped back into the ROI, and pixels outside the ROI were set to black.

Analysis of average calcium signals (ΔF/F) in identified glomeruli

To quantify average LN activity in Figure 1E, we averaged the images evoked by all four odor stimuli in each odor set. Each imaging plane in each experiment was treated separately. To identify the boundaries of glomeruli, we acquired high-resolution images of resting GCaMP fluorescence (512×512 pixels) at the conclusion of each experiment. We compared these images with published three-dimensional maps (Laissue et al., 1999), and we analyzed only those glomeruli which we could identify with reasonable confidence. Overall, however, our qualitative conclusions appear to generalize to other glomerular compartments which we could not confidently identify.

Each measurement of %ΔF/F was normalized to the maximum glomerulus in that brain. Thus, each brain contributed equally when values were averaged across brains. We note that for the three imaging planes that contain most of the glomeruli in this study (-12 μm, -24 μm, and -36 μm), there is no correlation between average LN activity in the antennal lobe across all odors and depth (R^2=0.0047, p=0.66). However, at the -48 μm plane (which contains VL1 and V), we observed significantly less antennal lobe LN activity across all odors than in the other imaging planes. This observation may reflect a true difference in the level of LN activity in the most ventral glomeruli as compared to other glomeruli, and/or an artifact of light scattering at the deepest imaging plane. Note that all but two of the glomeruli in Figure 1E are outside of this deepest imaging plane.

Analysis of LN anatomical data

Within a given series of brains (LNs expressing bruchpilot:GFP, n-synaptobrevin:GFP, or cytoplasmic GFP), images of all antennal lobes were collected with identical laser power, detector gain, and detector offset. Brains in which > 0.01% of antennal lobe pixels were saturated or below the detector offset (in areas that did not contain cell bodies or large primary neurites) were rejected. LN innervation and presynaptic release site density were quantified in Fiji (http://fiji.sc/Fiji), an Open Source image processing software based on ImageJ, using the Segmentation Editor plugin (J. Schindelin, F. Kusztos, B. Schmid). For selected glomeruli, three-dimensional boundaries were defined by manually tracing an ROI around the neuropil boundaries of each glomerulus in the nc82 signal of every third slice, and then interpolating through the stack to obtain the boundaries in adjacent slices. We wrote scripts to extend the functionality of the Segmentation Editor plugin by 1) allowing for the simultaneous tracking of multiple glomeruli across slices; and 2) automating the labeling of ROI coordinates and pixel intensities corresponding to different glomeruli when writing to file. Measurements were computed by dividing the total signal intensity (summed across all pixels in the three-dimensional ROI) by the number of pixels in the three-dimensional ROI. Measurements were normalized by the maximum glomerulus in each brain; thus, each brain contributed equally when values were averaged across brains.

Quantification of sEPSC suppression (% sEPSC activity)

For both GABA uncaging and LN optogenetic experiments, the effect of light on sEPSC activity was quantified as the ratio of the standard deviation (SD) of the current during the light pulse to that during the baseline period. Current traces were high-pass filtered at 4 Hz to remove slow baseline drift, and the SD during the light pulse was taken as the average of the SDs of individual 50 msec, non-overlapping epochs that span the light pulse. Similarly, the SD of the baseline period was taken as the average of the SDs of individual 50 msec, non-overlapping epochs that span three randomly chosen seconds of the baseline. Three seconds were used to improve our estimate of the baseline SD. Thus, for each trial, we calculated the ratio of the SD during light to the baseline SD. For each condition or light intensity, this ratio of $SD_{light}:SD_{baseline}$ was averaged across 5-6 trials and multiplied by 100. These values are referred to as “% sEPSC activity”.

To obtain a single metric that captures the sensitivity to GABA (or sensitivity to LN activation) of each cell, we fit a line to the average SD_{light}:$SD_{baseline}$ at each light intensity plotted against the light intensity, constraining this ratio to be 1 at zero light intensity. We took the slope of this line to be a metric of inhibition, with more negative slopes corresponding to more inhibited cells. Across all PNs, we then normalized the slope values so that the most negative slope (the cell most sensitive to GABA, or the cell most sensitive to LN activation) had a sensitivity of 1.

We also used an independent method to confirm the effectiveness of using SD to measure the effect of GABA or LN activation on sEPSC activity. For three cells which varied widely in their sensitivity to LN activation as measured above, we quantified sEPSCs by automated detection of individual sEPSCs, followed by manual visual inspection of detected events, as described previously (Gaudry et al., 2013). Using this method, we obtained results that were similar to the results using SD_{light}:$SD_{baseline}$. Event detection appeared to be noisier than SD_{light}:$SD_{baseline}$ in measuring the level of suppression, as evidenced by the larger trial-to-trial fluctuations associated with this measurement. Since the measurement of SD was also easier to implement, we chose to use SD_{light}:$SD_{baseline}$ to quantify these effects.

All analysis of sEPSC activity was performed blind to the glomerular identity of the PN. We observed no correlation between input resistance and either sensitivity to LN activation (R^2=5×10^{-4}, p=0.88), or sensitivity to GABA (R^2=0.012, p=0.45). Furthermore, we observed no correlation between average $SD_{baseline}$ and sensitivity to LN activation (R^2=0.008, p=0.62), or sensitivity to GABA (R^2=0.02, p=0.33). In addition, for the three cells described above in which we also used event detection to quantify sEPSC activity, we saw no systematic relationship between sensitivity to LN activity and either sEPSC amplitude or rate. These observations indicate that our measurement of sEPSC is not sensitive to glomerulus-to-glomerulus variations in the intrinsic characteristics of spontaneous activity.

In addition, we took advantage of the intrinsic suppression of sEPSC activity to extremely high levels of light to perform an additional control. For a significant subset of PNs which were qualitatively insensitive to LN activation or GABA (as measured during the course of the regular experiment), we exposed them to a pulse of high intensity light (>45 mW/mm^2 for 488 nm light, >35 mW/mm^2 for 390 nm light) at the end of the experiment. In all cells, high intensity light elicited artifactual, near-complete inhibition of sEPSC activity, directly demonstrating our ability to detect inhibition even in "insensitive" PNs.

Quantification of odor selectivity

Lifetime sparseness for each odorant receptor (and its corresponding glomerulus) was computed from odor-evoked ORN firing rates reported previously (Hallem and Carlson, 2006) according to the following equation (Vinje and Gallant, 2000):

$$s = \frac{1}{1-\frac{1}{n}}\left(1 - \frac{\left(\sum_{j=1}^{n}\frac{r_j}{n}\right)^2}{\sum_{j=1}^{n}\frac{r_j^2}{n}}\right)$$

where n is the number of odors and r_j is the odor response of the neuron to odor j (in spikes/s) minus the baseline firing rate. Negative firing rates were set to zero for the purposes of this analysis. Data for glomeruli DA1 and DA2 are not included in the Hallem data set, so we set the sparseness values for these glomeruli to 1 based on their reported extremely narrow odor tuning (Clyne et al., 1997; Stensmyr et al., 2012).

Odorant receptors were matched with glomeruli using published maps (Couto et al., 2005; Fishilevich and Vosshall, 2005). The Euclidean distance between the odor responses of a pair of glomeruli was computed in Matlab as the norm of the difference vector between the tuning profiles of the two odorant receptors in question, again using tuning profiles from the Hallem data set. PCA of odor response profiles was computed in Matlab, with the inputs being the mean-subtracted firing rates of the corresponding ORN types to the panel of odorants. The first three principal components of odor response space (PC1-PC3) account for the majority (64%) of the variance in odor responses.

Statistics

All group data represent mean ± SEM across experiments, except where otherwise noted. Statistics were computed using the Statistics toolbox in Matlab and in Excel. For one-way ANOVA of sensitivity to GABA or sensitivity to LN activity across glomeruli, we assumed that data are normally distributed (distributions fail the Lilliefors test for non-normality at the $p=0.01$ level). However, a non-parametric statistical test also indicates that the mean values of different glomeruli are significantly different (sensitivity to GABA, Kruskal-Wallis test, $p=0.003$; sensitivity to LN activity, Kruskal-Wallis test, $p=0.03$).

For experiments with unequal errors in the x- and y-axes (i.e. sensitivity to LN activation versus sensitivity to GABA), p-values were computed using a permutation analysis. For data on each axis, we randomly shuffled the data points with their glomerular labels, recomputed the means for each glomerulus, and calculated a correlation coefficient (R) using the new glomerular means. Data was permuted 10^6 trials for each analysis. The p-value was calculated as the proportion of trials in which R^2 was greater than or equal to the observed R^2 from the true glomerular labels. This analysis has the advantage of being simple, is robust to unequal numbers of observations in each category, and makes no assumptions about the underlying distribution of the data on each axis.

Two general categories of correlations were performed across glomeruli: (1) those that correlated variables relating to the mechanism of sensitivity to LN activation (Figures 6A, 6C, 8D, S4, and related text), and (2) those that correlated variables related to the function of inhibition (i.e. with respect to odor tuning; Figure 9B-E and related text). Within each category, the Bonferroni-corrected threshold for significance to account for multiple comparisons at a 5% error rate is $p<0.008$ for category 1 and $p<0.004$ for category 2. We did not alter the p-values in the text to correct for multiple comparisons (except in Figure 2C); rather, we reported correlations as significant only if they had p-values less than the Bonferroni-corrected thresholds.

References for Supplemental Experimental Procedures

Baird, D.H., Schalet, A.P., and Wyman, R.J. (1990). The Passover locus in Drosophila melanogaster: complex complementation and different effects on the giant fiber neural pathway. Genetics *126*, 1045-1059.

Berdnik, D., Chihara, T., Couto, A., and Luo, L. (2006). Wiring stability of the adult Drosophila olfactory circuit after lesion. J. Neurosci. *26*, 3367-3376.

Bhandawat, V., Olsen, S.R., Schlief, M.L., Gouwens, N.W., and Wilson, R.I. (2007). Sensory processing in the Drosophila antennal lobe increases the reliability and separability of ensemble odor representations. Nat. Neurosci. *10*, 1474-1482.

Chou, Y.H., Spletter, M.L., Yaksi, E., Leong, J.C., Wilson, R.I., and Luo, L. (2010). Diversity and wiring variability of olfactory local interneurons in the Drosophila antennal lobe. Nat Neurosci *13*, 439-449.

Clyne, P., Grant, A., O'Connell, R., and Carlson, J.R. (1997). Odorant response of individual sensilla on the Drosophila antenna. Invert. Neurosci. *3*, 127-135.

Couto, A., Alenius, M., and Dickson, B.J. (2005). Molecular, anatomical, and functional organization of the Drosophila olfactory system. Curr. Biol. *15*, 1535-1547.

Estes, P.S., Ho, G.L., Narayanan, R., and Ramaswami, M. (2000). Synaptic localization and restricted diffusion of a Drosophila neuronal synaptobrevin--green fluorescent protein chimera in vivo. J Neurogenet *13*, 233-255.

Fishilevich, E., and Vosshall, L.B. (2005). Genetic and functional subdivision of the Drosophila antennal lobe. Curr. Biol. *15*, 1548-1553.

Gaudry, Q., Hong, E.J., Kain, J., de Bivort, B.L., and Wilson, R.I. (2013). Asymmetric neurotransmitter release enables rapid odour lateralization in Drosophila. Nature *493*, 424-428.

Gouwens, N.W., and Wilson, R.I. (2009). Signal propagation in Drosophila central neurons. J Neurosci *29*, 6239-6249.

Halfon, M.S., Gisselbrecht, S., Lu, J., Estrada, B., Keshishian, H., and Michelson, A.M. (2002). New fluorescent protein reporters for use with the Drosophila Gal4 expression system and for vital detection of balancer chromosomes. Genesis *34*, 135-138.

Hallem, E.A., and Carlson, J.R. (2006). Coding of odors by a receptor repertoire. Cell *125*, 143-160.

Hwang, R.Y., Zhong, L., Xu, Y., Johnson, T., Zhang, F., Deisseroth, K., and Tracey, W.D. (2007). Nociceptive neurons protect Drosophila larvae from parasitoid wasps. Curr. Biol. *17*, 2105-2116.

Laissue, P.P., Reiter, C., Hiesinger, P.R., Halter, S., Fischbach, K.F., and Stocker, R.F. (1999). Three-dimensional reconstruction of the antennal lobe in Drosophila melanogaster. J. Comp. Neurol. *405*, 543-552.

Lee, T., and Luo, L. (1999). Mosaic analysis with a repressible cell marker for studies of gene function in neuronal morphogenesis. Neuron *22*, 451-461.

Ng, M., Roorda, R.D., Lima, S.Q., Zemelman, B.V., Morcillo, P., and Miesenbock, G. (2002). Transmission of olfactory information between three populations of neurons in the antennal lobe of the fly. Neuron *36*, 463-474.

Olsen, S.R., Bhandawat, V., and Wilson, R.I. (2007). Excitatory interactions between olfactory processing channels in the Drosophila antennal lobe. Neuron *54*, 89-103.

Olsen, S.R., Bhandawat, V., and Wilson, R.I. (2010). Divisive normalization in olfactory population codes. Neuron *66*, 287-299.

Pfeiffer, B.D., Jenett, A., Hammonds, A.S., Ngo, T.T., Misra, S., Murphy, C., Scully, A., Carlson, J.W., Wan, K.H., Laverty, T.R., *et al.* (2008). Tools for neuroanatomy and neurogenetics in Drosophila. Proc Natl Acad Sci U S A *105*, 9715-9720.

Pologruto, T.A., Sabatini, B.L., and Svoboda, K. (2003). ScanImage: flexible software for operating laser scanning microscopes. Biomedical engineering online *2*, 13.

Schmid, A., Hallermann, S., Kittel, R.J., Khorramshahi, O., Frolich, A.M., Quentin, C., Rasse, T.M., Mertel, S., Heckmann, M., and Sigrist, S.J. (2008). Activity-dependent site-specific changes of glutamate receptor composition in vivo. Nat Neurosci *11*, 659-666.

Stensmyr, M.C., Dweck, H.K., Farhan, A., Ibba, I., Strutz, A., Mukunda, L., Linz, J., Grabe, V., Steck, K., Lavista-Llanos, S., *et al.* (2012). A conserved dedicated olfactory circuit for detecting harmful microbes in Drosophila. Cell *151*, 1345-1357.

Sweeney, L.B., Couto, A., Chou, Y.H., Berdnik, D., Dickson, B.J., Luo, L., and Komiyama, T. (2007). Temporal target restriction of olfactory receptor neurons by Semaphorin-1a/PlexinA-mediated axon-axon interactions. Neuron *53*, 185-200.

Tian, L., Hires, S.A., Mao, T., Huber, D., Chiappe, M.E., Chalasani, S.H., Petreanu, L., Akerboom, J., McKinney, S.A., Schreiter, E.R., *et al.* (2009). Imaging neural activity in worms, flies and mice with improved GCaMP calcium indicators. Nat Methods *6*, 875-881.

Trigo, F.F., Corrie, J.E., and Ogden, D. (2009). Laser photolysis of caged compounds at 405 nm: photochemical advantages, localisation, phototoxicity and methods for calibration. J Neurosci Methods *180*, 9-21.

Vinje, W.E., and Gallant, J.L. (2000). Sparse coding and decorrelation in primary visual cortex during natural vision. Science *287*, 1273-1276.

Wilson, R.I., Turner, G.C., and Laurent, G. (2004). Transformation of olfactory representations in the Drosophila antennal lobe. Science *303*, 366-370.

Wilson, R.I., and Laurent, G. (2005). Role of GABAergic inhibition in shaping odor-evoked spatiotemporal patterns in the Drosophila antennal lobe. J. Neurosci. *25*, 9069-9079.

Yaksi, E., and Wilson, R.I. (2010). Electrical coupling between olfactory glomeruli. Neuron *67*, 1034-1047.